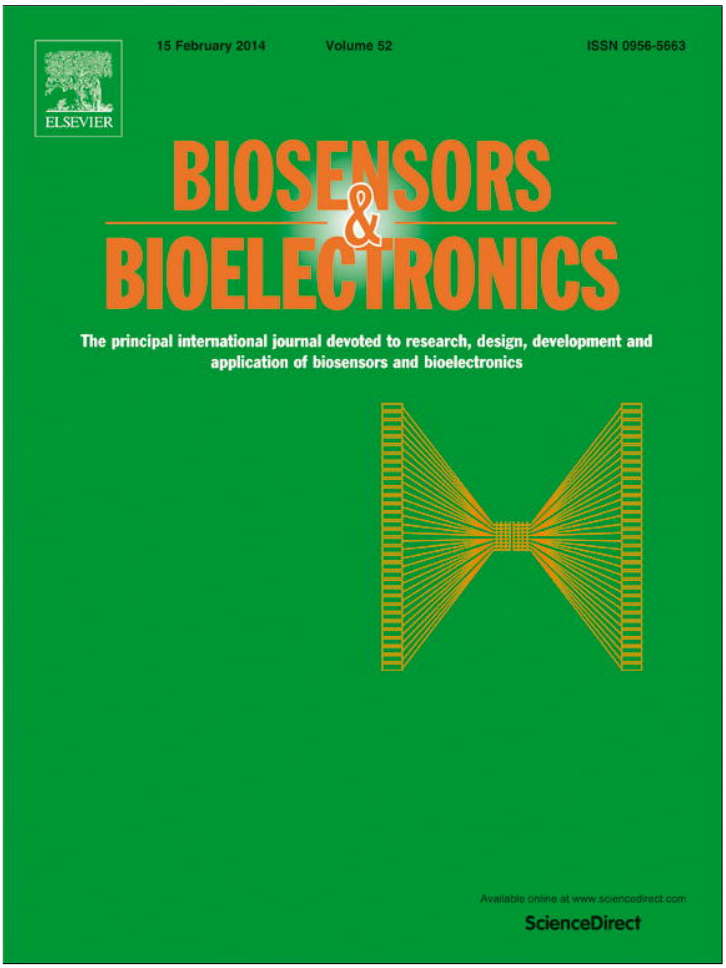

Biosensors and Bioelectronics 52 (2014) 232–238

Contents lists available at ScienceDirect

Biosensors and Bioelectronics

journal homepage: www.elsevier.com/locate/bios

Monitoring intracellular calcium in response to GPCR activation using thin-film silicon photodiodes with integrated fluorescence filters

S.A.M. Martins [a,b,c], G. Moulas [a,b], J.R.C. Trabuco [c], G.A. Monteiro [c,d], V. Chu [a,b], J.P. Conde [a,b,d], D.M.F. Prazeres [c,d,*]

[a] INESC Microsistemas e Nanotecnologias (INESC MN), Rua Alves Redol 9, 1000-029 Lisbon, Portugal
[b] IN-Institute of Nanoscience and Nanotechnology, Rua Alves Redol 9, 1000-029 Lisbon, Portugal
[c] IBB—Institute for Biotechnology and Bioengineering, Instituto Superior Técnico, Avenida Rovisco Pais, 1049-001 Lisbon, Portugal
[d] Department of Bioengineering, Instituto Superior Técnico, 1049-001 Lisbon, Portugal

ARTICLE INFO

Article history:
Received 19 June 2013
Received in revised form
11 August 2013
Accepted 12 August 2013
Available online 5 September 2013

Keywords:
GPCR
Cell
Fluorescence
Calcium
Amorphous silicon
Integrated detection

ABSTRACT

G-protein coupled receptor (GPCRs) drug discovery is a thriving strategy in the pharmaceutical industry. The standard approach uses living cells to test millions of compounds in a high-throughput format. Typically, changes in the intracellular levels of key elements in the signaling cascade are monitored using fluorescence or luminescence read-out systems, which require external equipment for signal acquisition. In this work, thin-film amorphous silicon photodiodes with an integrated fluorescence filter were developed to capture the intracellular calcium dynamics in response to the activation of the endogenous muscarinic M1 GPCR of HEK 293T cells. Using the new device it was possible to characterize the potency of carbachol (EC_{50}=10.5 μM) and pirenzepine (IC_{50}=4.2 μM), with the same accuracy as standard microscopy optical systems. The smaller foot-print provided by the detection system makes it an ideal candidate for the future integration in microfluidic devices for drug discovery.

1. Introduction

The use of cells in biosensing and assaying often relies on the ability of their natural chemical receptors to respond to small variations in the quantities of target molecules in the surrounding environment. In eukaryotic cells, G-protein coupled receptors (GPCRs) comprise one of the largest classes of such receptors (Lagerstrom and Schioth, 2008; Lefkowitz, 2007). Ligand binding to GPCRs induces conformational changes on the receptor which leads to the activation of a transducer, a heterotrimeric G protein. The latter, in turn, activates an effector enzyme with the subsequent generation of second messenger molecules such as inositol triphosphate (IP3), calcium (Ca^{2+}) or cyclic adenosine monophosphate (cAMP), that alter cell activity (Eglen et al., 2007). GPCRs are thus extremely important targets for drug design, accounting for more than 30% of the pharmaceutical molecules currently available (Hopkins and Groom, 2002). Moreover, specific ligands have not yet been identified for more than 100 GPCRs (orphan GPCRs) (Kenakin, 2009; Schlyer and Horuk, 2006). Given this context, the ability to screen libraries of compounds for potential GPCR-acting molecules is crucial.

While the use of *in silico* approaches based on receptor structure models or computational approaches for rational drug design are emerging (Lagerstrom and Schioth, 2008; Shoichet and Kobilka, 2012), the current GPCR drug discovery programs are supported by the screening of millions of small molecule libraries either in high throughput (HTS) or high content (HCS) screening formats (Sewing and Cawkill, 2007). Historically, radioligand binding assays were the method of choice for the identification of compounds that bind to GPCR. Albeit sensitive, the relatively high costs, the limited compatibility with high throughput formats and hazardous protocols have prompted the development of non-radioactive alternatives (Zhang and Xie, 2012). Thus, and apart from the recently introduced label-free systems (Kenakin, 2009; Scott and Peters, 2010), technologies currently established rely on fluorescence or luminescence reporter systems to access the different levels of GPCR signaling (Boehme and Beck-Sickinger, 2009), ranging from the ligand binding event (Zwier et al., 2010) to functional assays whereby second messenger accumulation, receptor desensitization or reporter activation is monitored in living cells (Eglen, 2005; Inoue et al., 2012; Zhang and Xie, 2012). Amongst the available assays, fluorescence detection of intracellular calcium following activation of Gαq/11 coupled receptors

* Corresponding author at: IBB—Institute for Biotechnology and Bioengineering, Instituto Superior Técnico, Avenida Rovisco Pais, 1049-001 Lisbon, Portugal. Tel.: +351 218419133; fax: +351 218419062.
E-mail address: miguelprazeres@ist.utl.pt (D.M.F. Prazeres).

0956-5663/$ - see front matter © 2013 Elsevier B.V. All rights reserved.
http://dx.doi.org/10.1016/j.bios.2013.08.037

constitutes a stamp for current HTS assays. Typically, recombinant cell lines are cultured on microtiter plates (96–1536-wells) and stained with calcium sensitive dyes that exhibit enhanced fluorescence upon calcium binding. Test compounds are then added to the cell system and the generated calcium transients are monitored in real time (Hodder et al., 2004; Marshall et al., 2006). Successful attempts to couple non-Gαq receptors (e.g., Gαs or Gαi) by using cell lines expressing promiscuous G_{15} and G_{16} proteins have also been demonstrated (Kostenis et al., 2005), which makes calcium mobilization assays attractive to probe a variety of GPCRs. However one major drawback of such functional screens is the dependency on external and expensive systems for signal acquisition like laser scanners, microscopes or charge coupled devices (CCD). Moreover, as miniaturization of cell-based assays for drug screening systems through microfluidics is gaining momentum (Martins et al., 2012), the demand for new detection strategies compatible with the low culture volumes and reduced cell numbers provided by such systems is increasing (Kamei et al., 2003).

Recently, the use of hydrogenated amorphous silicon (a-Si:H) photosensors for fluorescence, chemiluminescence and colorimetric detection of biomolecules have been reported (Conde et al., 2008). Applications include the detection of DNA sequences (Kamei et al., 2005) and DNA hybridization (Pimentel et al., 2008), antibody/antigen recognition (Pereira et al., 2011), detection of food toxins (Caputo et al., 2012; Novo et al., 2012), detection of green fluorescence protein expression (Joskowiak et al., 2011) and detection of intrinsic fluorophores in bacterial systems (Joskowiak et al., 2012). These sensors are characterized by high quantum efficiencies in the range of visible light and lower dark currents when compared to crystalline silicon (Kamei et al., 2003). Additionally, a-Si:H films are compatible with microfabrication techniques and thus easily integrated into microfluidic devices, opening up prospects for the fabrication of miniaturized monolithic devices with potential gains in assay sensitivity, reproducibility and time (Novo et al., 2012).

In this work, the feasibility of using a-Si:H photodiodes with integrated absorption filters to detect calcium dynamics inside living mammalian cells cultivated *in vitro* via the calcium-sensitive fluorescent dye Fluo-4 (Gee et al., 2000) is demonstrated. Intracellular calcium (iCa^{2+}) fluxes are generated by stimulating cultured HEK 293T cells with chemical compounds that either: (i) permeabilize cell membranes to Ca^{2+} (ionomycin) or (ii) interact with the endogenous muscarinic M1 GPCR (Thomas and Smart, 2005) (carbachol and pirenzepine). The changes in fluorescence are detected using a-Si:H photodiodes with an integrated fluorescence filter and compared with those obtained by fluorescence microscopy.

2. Materials and methods

2.1. Chemicals and reagents

Fibronectin, carbachol and pirenzepine were purchased from Sigma. The calcium indicators Fluo-4 salt, Fluo-4 AM, Fluo-4 Direct and the reagents ionomycin calcium salt, probenecid, and calcium calibrated solutions were from Molecular Probes. Hank's balanced solution (HBSS: 1.26 mM $CaCl_2$, 0.493 mM $MgCl_2$, 0.407 mM $MgSO_4$, 5.33 mM KCl, 137 mM NaCl, 0.338 mM Na_2HPO_4, 5.5 mM D-glucose), 4-(2-hydroxyethyl)-1-piperazineethanesulfonic acid (10× HEPES) and cell culture reagents were purchased from GIBCO. Sylgard® 184 polydimethyl siloxane (PDMS) and the corresponding curing agent were purchased from Dow Corning. Human Embryonic kidney (HEK) 293T cell line was from American type culture collection, ATTC (ATTC® CRL-11268).

2.2. Measurement apparatus

2.2.1. Microscopy

Microscopy studies were performed using an inverted Olympus CKX41 fluorescence microscope equipped with a mercury arc lamp HBO 50 W (OSRAM) for illumination and band-pass filters in the range of 460–490 nm. Images were acquired with a Plan CN 10× objective. Real-time imaging recording was performed using the XC30 CCD camera and the acquisition software cellSens® from Olympus. Exposure time and gain were set to 1 s and 6 db, respectively, and real-time recordings were acquired for 250 s at a rate of 1 frame/s.

2.2.2. Amorphous silicon (a-Si:H) photodiodes with integrated fluorescence filter

The a-Si:H p-i-n photodiodes with integrated fluorescence filters were fabricated from glass substrates (AF45, Schott). Fabrication started with the deposition of a 2 μm thick amorphous silicon carbon alloy film (a-SiC:H) as the optical absorption filter by radio frequency plasma enhanced chemical vapor deposition (RF-PECVD), using deposition temperature and pressure of 100 °C and 0.1 Torr, respectively. Silane (SiH_4) and ethylene (C_2H_4) gas flows were set to 9.9 and 0.9 sccm, respectively, in order to control the carbon content of the film and hence, its optical characteristics (Lipovsek et al., 2010). The transmittance properties of the filter were characterized by illuminating the sample from the glass side, using a tungsten–halogen lamp (250 W) coupled to a monochromator (McPherson 2035) for wavelength selection (650–400 nm). The sample was vertically aligned with a crystalline silicon (c-Si) photosensor with known responsivity (Advanced Photonics) and the generated current was quantified using a picoammeter (Keithley 237). A reference sample (bare glass), was used as control. The fabrication of the photodiodes proceeded with the deposition, by sputtering, of indium tin oxide (ITO) as the transparent, bottom electrode (1000 Å). The a-Si:H p-i-n layers were obtained by sequentially depositing 200 Å of p-doped a-Si:H, 5000 Å of intrinsic a-Si:H and 200 Å n-doped a-Si:H using RF-PECVD, at 250 °C and 0.1 Torr. Diborane (B_2H_6) and phosphine (PH_3) were the source gases for the p- and n-layer, respectively. The top contact consisted of 150 Å film of titanium tungsten (TiW) and 1000 Å of aluminum (Al), deposited by sputtering, using a physical mask to define an array of 48 contacts. Each contact presented an area of 2 mm^2 and constituted the actual sensing unit of the device (Fig. 1A). The optoelectronic properties of the device were characterized by evaluating the current density–voltage (*J*–*V*) response,

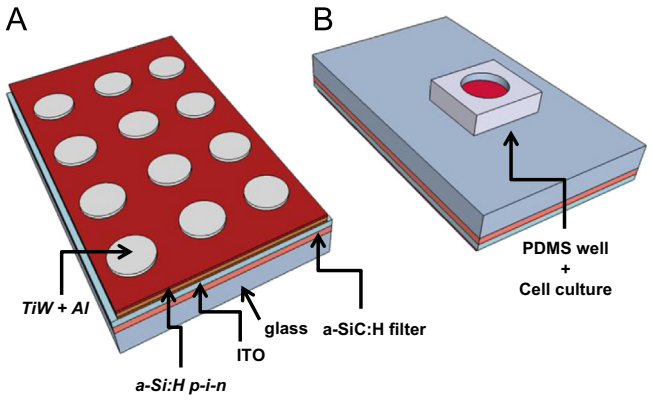

Fig. 1. (A) Schematic representation of the cross-section of an a-Si:H p-i-n photodiode with integrated a-SiC:H fluorescence filter. (B) Configuration used to measure the fluorescence of calcium solutions and cell cultures showing a PDMS well aligned with the photodiode from the glass side.

the external quantum efficiency (*EQE*) in the range 400–650 nm and detection limits (current density *J*, *versus* incident photon flux Φ). The *EQE* was determined using Eq. (1) where J_{ph} is the photocurrent density ($A\,cm^{-2}$), Φ is the incident photon flux ($cm^{-2}\,s^{-1}$), and *q* is the electron charge (1.60×10^{-19} C)

$$EQE=\frac{J_{ph}}{\phi q} \tag{1}$$

The light source was either the tungsten–halogen lamp coupled to the monochromator or a light emitting diode (LED), with a peak emission wavelength at 470 nm, coupled to a 500 nm shortpass filter (Thorlabs) as the excitation light. For the determination of the photon flux Φ, the calibrated c-Si photosensor was used under the same illumination conditions.

2.3. Fabrication of PDMS wells

PDMS wells were fabricated by pouring a mixture of the polymer and curing agent at a 10:1 ratio into a Petri dish and promoting curing for 2 h at 70 °C. The cured PDMS was cut in $1\times1\,cm^2$ (~1 cm height) and punched in the center to form 0.5 cm diameter wells. 100 μm-thick PDMS sheets were fabricated by spin-coating (Laurell Technologies) the polymer on cleaned silicon wafers (WRS materials) and curing for 2 h at 70 °C. The sheets were cut in $1\times1\,cm^2$ and used to seal the bottom of the wells by performing corona discharge ionization (Electro-Technique Products, Corona tester BD 20-AC) for 20 s.

2.4. Fluorescence and photocurrent measurements of calcium-calibrated solutions

Fifty microliters of solutions containing defined concentrations of calcium ions (0–1.35 μM Ca^{2+}) were prepared from calcium calibrated solutions (Molecular Probes) according to the manufacturers' instructions and incubated with a 4 μM solution of Fluo-4 salt prepared in a Ca^{2+}-free buffer (10 mM K_2EGTA). The fluorescence measurements were conducted on a Cary Eclipse spectrofluorometer (Varian) equipped with a microplate stage. The photomultiplier tube (PMT) voltage was set to 600 V, and excitation and emission filters to 490 and 516 nm, respectively, as required by the optical characteristics of Fluo-4 in the presence of 1.35 μM Ca^{2+}.

For the photocurrent measurements, PDMS wells containing 50 μL of each Ca^{2+} standard solution were aligned from the glass side (Fig. 1B) with the photodiode. The LED was used as the excitation light source. The measured current, *I*, was acquired using the picoammeter and converted to current density according to the area of the photodiodes (2 mm^2). Signals were normalized to the maximum value for comparison between the spectrofluorometer and photodiode measurement setups.

2.5. Cell culture and stimulation assays

HEK 293T cells (3×10^6 cells) were seeded in T75 cell culture flasks with 10 mL of Dulbeco's Modified Eagle's medium (DMEM), supplemented with 10% fetal bovine serum (FBS) and 1% antibiotic–antimycotic solution (penicillin, streptomycin and Fungizone®) and incubated at 37 °C in a 5% CO_2 atmosphere until reaching 80% confluence (~ 4 days). For microscopy monitoring of stimulation assays, cells were detached by incubation with trypsin–0.05% EDTA, seeded into cell-culture microtiter plates (Becton–Dickinson) at a density of 50×10^3 cells/well (50 μL) and allowed to adhere and spread for 16 h at 37 °C in a 5% CO_2 atmosphere. The adhered cells were subsequently incubated for 30 min at 37 °C with solutions of Fluo-4 Direct or 4 μM Fluo-4 AM prepared in assay buffer (1x HBSS, 20 mM HEPES supplemented with 2.5 mM probenecid) and then for 30 min at room temperature, in the dark. Test compounds (ionomycin, carbachol and pirenzepine) were prepared fresh, and diluted in assay buffer in such a way as to provide effective concentrations inside the wells of the order of 10^{-5}–10^{-8} M for ionomycin and 10^{-2}–10^{-8} M for carbachol and pirenzepine. The microtiter plate was mounted on the microscope stage and the baseline fluorescence was acquired for 20–50 s. Addition of test compounds (20 μL) was performed manually with the aid of a pipette and the change in fluorescence was monitored throughout the following 200 s. In the pirenzepine assays, fluorescence was monitored for 5 min after addition of pirenzepine. Carbachol (EC_{80}) was then added and fluorescence signals were monitored for 200 s. Negative controls were performed by injecting 20 μL of assay buffer.

For the photodiode monitoring of stimulation assays, PDMS wells were first treated with 100 μg/mL of fibronectin for 1 h, at 37 °C. The wells were rinsed with phosphate buffer and kept at 4 °C until further use. On the day of the stimulation assays, cells were seeded on the PDMS wells (75×10^3 cells/well in a total volume of 50 μL) and allowed to adhere and spread for 1 h, at 37 °C, under a 5% CO_2 atmosphere. Incubation with the calcium sensitive dyes was performed as described above. The cell-containing PDMS wells were then aligned with the photodiodes from the glass side (Fig. 1B), and illuminated vertically using the LED coupled to a 500 nm shortpass filter. The baseline signal was acquired for 20–50 s using the picoammeter at 0 voltage bias. Test compounds (prepared as described above) were injected manually (20 μL) into the wells and the change in the photodiode's current was monitored for the following 200 s.

2.6. Data analysis

Time dependent light intensity was extracted from fluorescence real-time images (1 frame/s) using the ImageJ software (NIH). An in-house software was developed (Labview) for real-time current acquisition. A GPIB connection ensured communication with the Keithley picoammeter. Data were recorded every second as follows: 8 data points were acquired regularly with a 10 ms integration time. The averaged value was then sent to the computer. Under the illumination light conditions, the photodiode time response was measured in the 1–10 s range. Therefore, the software acquisition method was not considered as a limitation for the experiments. In the cell stimulation assays, the signals acquired in the first 20–50 s (prior to compound injection) were averaged to obtain a baseline signal (S_0) and the response signals (S_i) were normalized according to $(S_i–S_0)/S_0$. Normalized responses were extracted as a function of the concentration of the stimulating compound and fit to a four parameter Hill dose response curve (no constraints), according to the following equation using the software GraphPad Prism®:

$$y=\frac{A1+(A2-A1)}{1+10^{[(LogEC50-x)*p]}} \tag{2}$$

where *y* is the response signal, *A*1 is the bottom asymptote (minimum response), *A*2 is the top asymptote (maximum response), *x* is the compound concentration, LogEC50 is the logarithm of the effective concentration which generates the half-maximum response and *p* is the Hill slope. In order to compare data obtained with the microscopy and photodiode measurement setups, the mean of the maximum response obtained with each setup was defined as 100%. Statistical analysis was performed by conducting a Fisher test for model comparison and unpaired *T* tests (GraphPad Prism®) for individual coefficient comparison. Signal to noise ratio (*S*/*N*) was determined according to Zhang et al. (1999).

3. Results and discussion

This work investigates the feasibility of using a-Si:H photodiodes integrated with absorption filters to detect calcium dynamics inside living mammalian cells cultivated *in vitro* via fluorescence monitoring.

3.1. Characterization of the a-Si:H p-i-n photodiodes with integrated fluorescence filter

A major challenge in fluorescence detection relies on the ability to discriminate between excitation and emission photons, while assuring that a maximum number of emission photons reach the detector. Previous work from our group has demonstrated the applicability of a-SiC:H alloy films as optical absorption filters for integrated fluorescence detection (Joskowiak et al., 2012). In this work, an a-SiC:H film with a carbon content of 8% (Lipovsek et al., 2010) was fabricated and integrated with a-Si:H p-i-n photodiodes. Excitation and emission spectra of Fluo-4 and the transmittance of the filter as a function of wavelength are depicted in Fig. S1 in supplementary data.

The efficiency of the photodiodes was characterized by determining the external quantum efficiency (*EQE*), a parameter that reflects the number of detected electrons as a function of incident photons (Pimentel et al., 2008). Fig. 2A shows the calculated *EQE* and the transmittance of the filter at relevant wavelengths. The filter presents low transmittance ($<0.001\%$), and hence high absorption, for wavelengths below 480 nm, becoming increasingly transparent as wavelength increases. At 490 nm (λEx of Fluo-4), only 0.013% of the photons are transmitted, whereas at 516 nm (λEm of Fluo-4), transmittance is $\sim$30 times higher. The *EQE* increases up to 600 nm as the number of photons impinging on the device increase (increased transmittance). The *EQE* at 516 nm is approximately 20 times higher than the *EQE* at 490 nm. Additionally, in the context of fluorescence detection and due to the characteristic broad bell-shaped emission spectrum of organic fluorophores such as Fluo-4, further gains in current are expected by collecting a fraction of the lower energy photons that are emitted at the higher wavelengths. For the higher wavelengths, the observed decrease in *EQE* can be explained by a decrease in absorption in the a-Si:H layers that constitute the p-i-n junction due to the characteristic a-Si:H energy band gap ($Eg\sim1.7$ eV) (Kamei et al., 2003).

The *J–V* response of different photodiodes, both in the dark and under illumination, was characterized and a representative *J–V* curve is shown in Fig. S2, supplementary data. At 0 V bias, the dark current density is as low as 0.1 nA cm^{-2}. Incident monochromatic light at 490 nm (490_{mch}) induces a 100 fold increase in the photodiode current density ($\sim$40 nA cm^{-2}), which is related to the transmittance of the filter at this wavelength. Still, the current generated at 526 nm is approximately 20 times higher in good agreement with the *EQE* values calculated above. At this point, the possibility of using a broadband LED, with a peak emission wavelength at 470 nm as the excitation light source was tested. Due to the characteristic spread around an LED peak wavelength (typically 40–90 nm) (Dandin et al., 2007), the LED was coupled to a shortpass filter in order to cut wavelengths above 500 nm. The power density of the incident LED light was calculated to be 6 mW cm^{-2} which results from 1.3×10^{16} cm^{-2} s^{-1} photon flux. These values contrast with the power density and photon fluxes obtained at 490_{mch} nm (0.25 mW cm^{-2} and 6.0×10^{14} cm^{-2} s^{-1}, respectively). However, at 0 V, the current generated by the LED on the p-i-n photodiode is 5 nA cm^{-2}, thus a smaller current is generated with a 20$\times$ increase in the photon flux when compared to 490_{mch} nm (Fig. 2B and Fig. S2 in supplementary data). This trend is explained by the low transmittance of the filter at 470 nm ($<0.001\%$) and the consequent reduced *EQE* values at this LED wavelengths. Fig. 2B also shows that the current density at λEm of Fluo-4 varies linearly within a wide range of photon fluxes ($10^{10}-10^{14}$ cm^2 s^{-1}), and that current intensities as low as 4 pA can be detected. Using the LED as the incident light source and due to the absorption proprieties of the integrated filter, improved ratios between $J_{\lambda Em}/J_{\lambda Ex}$ for higher values of Φ can be achieved. In view of this, the LED was selected as the excitation light source for the biological experiments.

3.2. Fluorescent detection of calcium ions in solution using the p-i-n photodiodes with an integrated fluorescence filter

The feasibility of using the a-Si:H photodiodes to detect calcium in combination with a fluorescent indicator was assessed first using calibrated calcium buffers. These buffers consist of standards of CaEGTA complexes that in equilibrium produce solutions of Ca^{2+} ions with defined concentrations that span the expected physiological range. These Ca^{2+} ions are free to react with the Fluo-4 salt, producing a fluorescence signal that is proportional to the Ca^{2+} concentration (Takahashi et al., 1999). Cells at rest have an iCa^{2+} concentration of 100 nM that can increase up to 10 times upon a stimulus (Berridge et al., 2000). Thus, standard Ca^{2+} solutions were prepared in the 0–1.35 μM concentration range (0, 0.017, 0.038, 0.1, 0.35, 0.6 and 1.35 μM). Fig. 3 compares the signal intensities obtained with the Fluo-4-induced fluorescence of Ca^{2+} standards measured using both the fabricated devices (closed squares) and a standard spectrofluorometer (open squares). Data were normalized to the maximum value to facilitate comparison. Results show that the intensities of the output signals from both systems increase as Ca^{2+} concentration increases. Background signals are slightly higher with the p-i-n

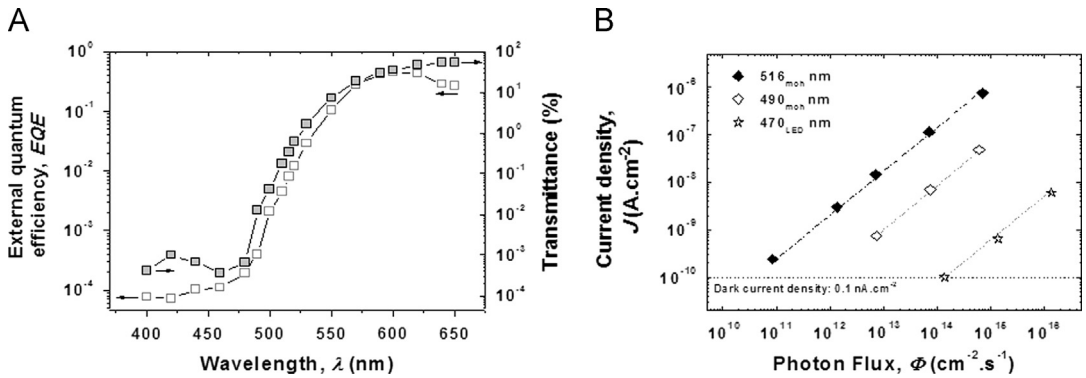

Fig. 2. Characterization of the a-Si:H p-i-n photodiodes with integrated fluorescence filter. (A) External quantum efficiency of the device, *EQE* (open squares, left axis) overlapping the optical transmission of the filter (closed squares, right axis). (B) Dependency of the device current (*J*) on the incident photon flux (Φ).

photodiode setup, mostly due to the contribution of incident photons to the generated current. This background signal is reduced in the spectrofluorometer plate reader due to the decoupling angle (90°) between the excitation beam and the emission channel. For this reason, the sensitivity as given by the inverse slope is also improved in the spectrofluorometer read-out. Nevertheless, the current densities of the p-i-n photodiodes varied approximately one order of magnitude (2×10^{-8}–2.6×10^{-7} A cm^{-2}), throughout the analyzed calcium concentration range, making their performance sufficient to be tested for iCa^{2+} monitoring.

3.3. Monitoring intracellular calcium dynamics using p-i-n photodiodes

As a first approach, HEK 293T cells were stimulated with different concentrations of ionomycin, an ionophore that renders the cell membranes permeable to Ca^{2+}. Since the extracellular calcium concentration is elevated with respect to the intracellular environment, stimulation with ionomycin leads to an increase in iCa^{2+}, as a result of transport of calcium ions from both the extracellular space and intracellular stores (Erdahl et al., 1994; Vasilev et al., in press).

In these studies cells were loaded with the ester form of Fluo-4 (Fluo-4-AM) which is cell permeable. Two different formulations of Fluo-4-AM were tested: a Fluo-4-AM solution and Fluo-4-Direct. The latter comprises a commercial formulation containing Fluo-4 and a quencher that prevents background fluorescence. Previous cell loading optimization assays revealed no significant differences between the two formulations up to 2 h of staining, although the use of Fluo-4-AM solution required a second wash to remove unloaded dye (results not shown). The response of cells to ionomycin was monitored in real-time using both the integrated photodetectors and a fluorescence microscope, for comparison. In the microscope measurements, the 10× objective provided ~1000 cells in the field of view, whereas in the p-i-n integrated device, the overall signal results from the contribution of all the cells adhering to the PDMS well. Microscopy images of cells before injection ($T=10$ s), after injection of ionomycin (5 μM effective concentration) in a Ca^{2+} containing buffer ($T=80$ s) and at the end of the experiment ($T=200$ s) are depicted in Fig. S3, supplementary data. At $T=10$ s, cells display a basal fluorescence as a result of the reaction of Fluo-4 with the iCa^{2+} ions characteristic of the cell's resting state. As expected, after ionomycin injection, the fluorescence of cells increased significantly due to an increase in iCa^{2+} and remained elevated until the end of the assay, most likely due to the establishment of an equilibrium between extracellular and intracellular calcium. In Fig. 4A, raw data collected from a representative real time analysis is provided for both the microscope and the integrated p-i-n photodiodes, confirming that the calcium dynamics is observable with both systems. The iCa^{2+} rise occurs a few seconds after ionomycin injection, as indicated by the steep rise in the photodiode's current and corroborated by the microscopy measurements. The signal plateau seen for $T>150$ s was not observed for ionomycin concentrations below 0.1 μM, suggesting that at these low concentrations the cell mechanisms to maintain calcium homeostasis are still functional (Kiselyov et al., 2003). Injection of the ionomycin solution caused some degree of perturbation in both systems probably due to interferences in the optical path. Furthermore, buffer addition evoked minor changes in both current and fluorescence, but the corresponding signals are significantly lower when compared to the ionomycin response (open symbols in Fig. 4B). The relative increase of the observed signals with respect to the basal level ($(S_i-S_0)/S_0$) reflects, though indirectly, changes in iCa^{2+} concentration, which in turn, are dependent on the magnitude of stimulus (Erdahl et al., 1994). Ionomycin dose-response curves obtained with the integrated devices and with the fluorescence microscope are represented on Fig. 4B. In order to compare the data obtained with the two setups, the average values of the maximum relative signal were defined as 100%. The $LogEC_{50}$ were calculated to be -6.31 ± 0.07 and -6.27 ± 0.1 for the p-i-n device and microscopy setup, equivalent to EC_{50} values (as calculated by the anti-log), of 0.48 and 0.54 μM, respectively. By performing

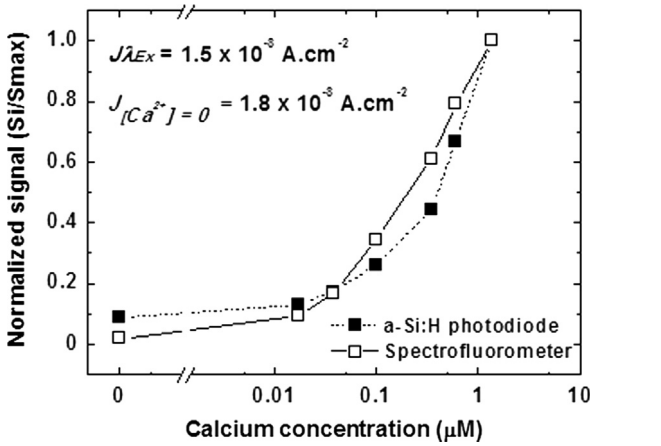

Fig. 3. Comparison of signal intensities obtained when measuring Fluo-4-induced fluorescence of Ca^{2+} standards with photodiodes (closed squares) and a standard spectrofluorometer (open squares). Data were normalized to the maximum value to facilitate comparison between the distinct setups (S_i/S_{max}).

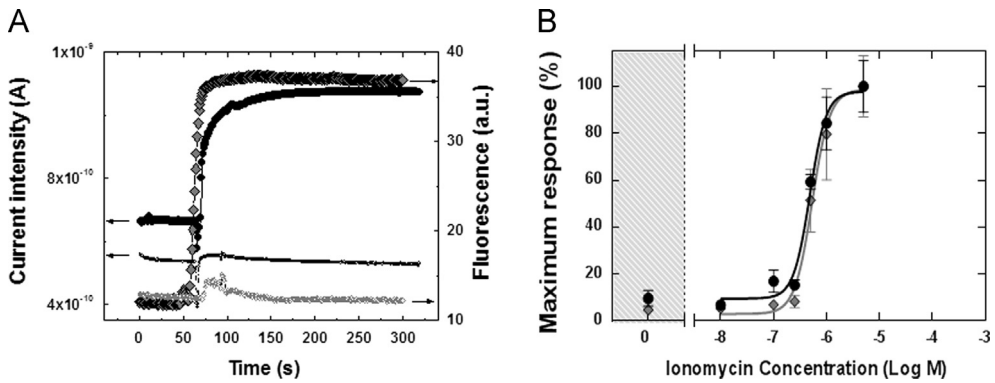

Fig. 4. (A) Representative real-time signals of calcium fluxes obtained using the microscope (diamonds) and the p-i-n a-Si:H device (circles) in response to 5 μM of ionomycin (closed symbols) and assay buffer (open symbols). (B) Dose response curves for ionomycin stimulation assays. Data represent averages and standard error of the mean (SEM). Diamonds: Microscopy data with $y=2.86-(98.6-2.86)/1+10^{((-6.27-x)*2)}$. $n=3$ independent assays. Circles: integrated devices with $y=9.41-(97.8-9.41)/1+10^{((-6.31-x)*2)}$. $n=4$ independent assays.

unpaired *T* tests for coefficient comparisons ($p < 0.05$ for statistical significance), no significant differences were obtained between the values of $LogEC_{50}$ ($p=0.17$). Additionally, by performing a Fisher test for model comparison, no statistically significant differences were obtained between the two curves ($p=0.9$). Hence, by using the a-Si:H photodiodes integrated with absorption filters it is possible to generate dose-response curves with the same accuracy as using the standard microscopy-based setup.

3.4. Characterization of endogenous M1 GPCR in a HEK293T cell line using p-i-n photodiodes

The possibility of using the integrated-filter p-i-n photodiodes for the characterization of GPCR signaling was investigated. The muscarinic type M1 receptor, which is endogenously expressed in the HEK 293T cell line, was chosen as the concept model (Thomas and Smart, 2005). In the intracellular environment, M1 is commonly coupled to the Gαq/11 type G-protein, which activates phospholipase C (PLC). Subsequently, IP3 is generated triggering the release of Ca^{2+} from the endoplasmic reticulum into the cytoplasm (Karakiulakis and Roth, 2012). In general, the iCa^{2+} fluxes are transient, characterized by a fast peak rise in iCa^{2+}, followed by a slow decay as desensitization of the GPCR occurs and the iCa^{2+} concentration is restored (Video 1 in supplementary data). Results shown in Fig. 5A represent a characteristic real-time analysis of HEK 293T cells stimulated with 1 mM of carbachol (an M1 agonist), confirming that the expected iCa^{2+} kinetics could be observed with the integrated p-i-n photodiodes. For a 1 mM stimulus, the device's current increased on average 28% with respect to the baseline ($n=8$ independent experiments), whereas negative controls ($n=6$ independent experiments), contributed on average to a 3.5% increase in the device's current. Higher increments over the baseline were observed using the fluorescence microscope setup, once again reflecting the different optical filtering capabilities (interference filter in the microscope) of the incident photons. Consequently, the *S*/*N* ratio is larger in the microscope ($S/N=20$) when compared to the p-i-n photodiode setup ($S/N=7.5$). Fig. 5B shows the dose-response curves of carbachol obtained using both measurements setups. The $LogEC_{50}$ was determined to be -4.98 ± 0.2 with the integrated device and -4.95 ± 0.10 with the microscope setup, which translates into EC_{50} values of 10.5 and 11.1 μM, respectively. These values are in good agreement with the EC_{50} values (4–11 μM) reported by other authors for HEK 293T endogenous M1 (Conklin et al., 1992; Mundell and Benovic, 2000). No significant statistical differences were observed between the different setups with regards to the calculated values of $LogEC_{50}$ ($p=0.4$) and the generated curves ($p=0.93$). Values of EC_{50} in the nanomolar range have been reported when using recombinant cell lines that overexpress the M1 GPCR (Liu et al., 2010). However, since in these recombinant cell systems the expression of cell surface receptors is increased over native cells, higher signals are typically obtained for lower compound dosage.

Finally, the specificity of the cell response observed upon carbachol stimulation was analyzed. The rationale behind this analysis is based on the fact that multiple receptor families are expressed in the HEK 293T cell line. Thus, agonist cross-reactivity among the different receptor families as well as endogenous ion-gated channels can contribute to calcium signaling independently from M1 activation. Pirenzepine, a well-known neutral antagonist of the M1 receptor with sub-type specificity (Piggott et al., 2002) was used in this study. The addition of pirenzepine to the cell culture is expected to specifically block M1 activation upon agonist addition in a dose response manner. Fig. 5B shows the dependency of the response signal as a function of the pirenzepine concentration in the cell culture and upon addition of carbachol at an EC_{80} concentration (0.05 mM). Results obtained with the photodiodes and fluorescence microscope show that maximum responses are obtained in the absence of pirenzepine. As pirenzepine concentration increases, the signal decreases according to a typical inhibitory dose response curve. It is possible thus to conclude that the transient signals produced upon carbachol addition (Fig. 5B) are derived from specific M1 activation. Data from the response curves was used further to determine values of Log IC_{50}, the Log of inhibitor concentration that reduces the maximum response by half. No significant differences ($p=0.4$) were observed between values obtained with the integrated p-i-n photodiodes

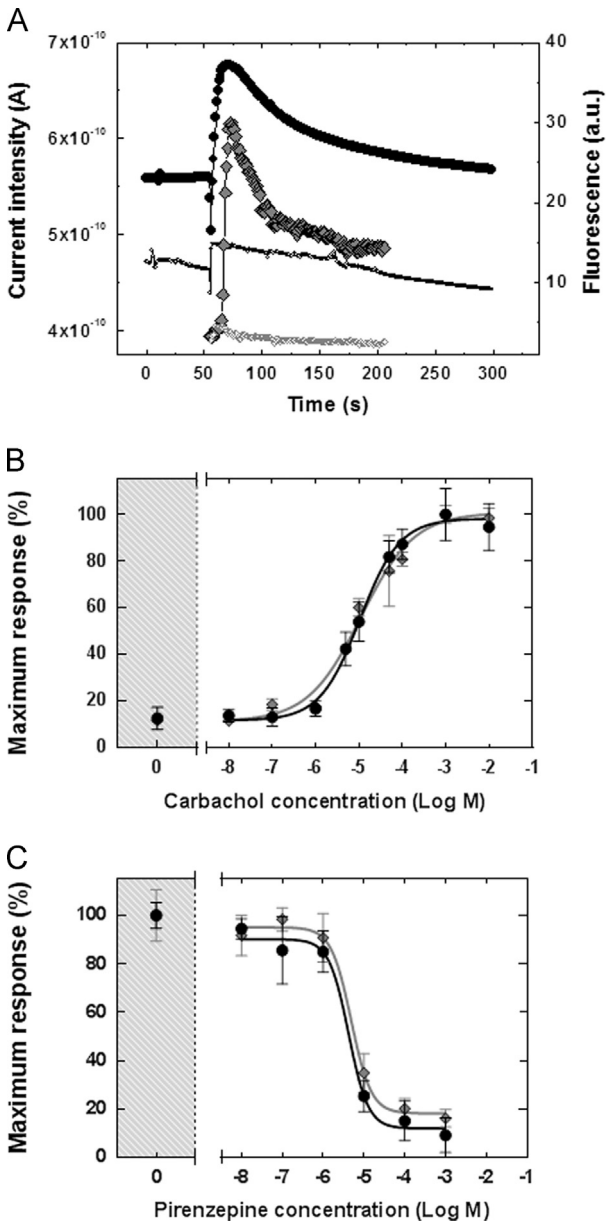

Fig. 5. (A) Representative real-time signals of calcium transient fluxes using the microscope (diamonds) and the p-i-n a-Si:H device (circles) in response to 1 mM carbachol (closed symbols) and assay buffer (open symbols). (B) Dose response curves for carbachol stimulation assays. Data represent averages and standard error of the mean (SEM). Diamonds: Microscopy data with $Y=11.3-(100-11.3)/1+10^{((-4.95-x)*0.7)}$. $n=4$ - 8 independent assays. Circles: integrated devices with $Y=11.8-(98.2-11.8)/1+10^{((-4.98-x)*0.9)}$. $n=4$–8 independent assays. (C) Dose response curves for pirenzepine inhibition assays. Data represent averages and standard error of the mean (SEM). Diamonds: Microscopy data with $Y=18.1-(95.0-18.1)/1+10^{((-5.31-x)*-1.7)}$. $n=3$ independent assays. Circles: integrated devices with $y=12-(12-90.1)/1+10^{((-5.40-x)*-1.8)}$. $n=3$–4 independent assays.

(Log $IC_{50} = -5.4 \pm 0.2$, $IC_{50} = 4.2$ μM) and with the fluorescence microscope (Log $IC_{50} = -5.3 \pm 0.2$, $IC_{50} = 4.9$ μM).

4. Conclusions

The possibility of using a-Si:H photodiodes with integrated fluorescence filters for the real-time evaluation of drug-induced changes in the levels of second messengers inside live cells was demonstrated. The devices developed were able to detect changes in iCa^{2+} concentration and identify different iCa^{2+} dynamics such as sustained plateaus or transient fluxes. Furthermore, dose-response profiles for both agonism and antagonism were established with the same accuracy as provided by standard optical systems. Most importantly, the challenge of detecting endogenous GPCRs that are usually expressed at lower densities was consistently met. The uniqueness of the a-Si:H devices relies on their compatibility with microfabrication techniques, making it possible to envisage the fabrication of micron-sized sensors that can easily be integrated into miniaturized cell platforms for drug screening. In particular, integration with microfluidic platforms that enable automatic fluid handling is expected to improve assay reproducibility with major impacts on the current *S*/*N* ratio.

Acknowledgments

S.A.M. Martins acknowledges FCT for Post-Doctoral Grant SFRH/BPD/66179/2009. G. Moulas acknowledges FCT for Post-Doctoral Grant SFRH/BPD/44425/2009. The authors acknowledge Simão Castro for the microscopic measurements using pirenzepine and Pedro Novo for advises on electronic measurements. This work is funded by the Fundação para a Ciência e a Tecnologia through the Associated Laboratories IN and IBB.

Appendix A. Supplementary material

Supplementary data associated with this article can be found in the online version at http://dx.doi.org/10.1016/j.bios.2013.08.037.

References

Berridge, M.J., Lipp, P., Bootman, M.D., 2000. Nature Reviews Molecular Cell Biology 1 (1), 11–21.
Boehme, I., Beck-Sickinger, A.G., Cell Communication and Signaling 7 http://dx.doi.org/10.4061/2011/460850, in press.
Caputo, D., de Cesare, G., Fanelli, C., Nascetti, A., Ricelli, A., Scipinotti, R., 2012. IEEE Sensors Journal 12 (8), 2674–2679.
Conde, J.P., Pimentel, A.C., Pereira, A.T., Gouvêa, A., Prazeres, D.M.F., Chu, V., 2008. Journal of Non-Crystalline Solids 354 (19–25), 2594–2597.
Conklin, B.R., Chabre, O., Wong, Y.H., Federman, A.D., Bourne, H.R., 1992. Journal of Biological Chemistry 267 (1), 31–34.
Dandin, M., Abshire, P., Smela, E., 2007. Lab on a Chip 7 (8), 955–977.
Eglen, R.M., 2005. Combinatorial Chemistry and High Throughput Screening 8 (4), 311–318.
Eglen, R.M., Bosse, R., Reisine, T., 2007. Assay and Drug Development Technologies 5 (3), 425–451.
Erdahl, W.L., Chapman, C.J., Taylor, R.W., Pfeiffer, D.R., 1994. Biophysical Journal 66 (5), 1678–1693.
Hodder, P., Mull, R., Cassaday, J., Berry, K., Strulovici, B., 2004. Journal of Biomolecular Screening 9 (5), 417–426.
Hopkins, A.L., Groom, C.R., 2002. Nature Reviews Drug Discovery 1 (9), 727–730.
Inoue, A., Ishiguro, J., Kitamura, H., Arima, N., Okutani, M., Shuto, A., Higashiyama, S., Ohwada, T., Arai, H., Makide, K., Aoki, J., 2012. Nature Methods 9 (10), 1021–1029.
Joskowiak, A., Santos, M.S., Prazeres, D.M.F., Chu, V., Conde, J.P., 2011. Sensors and Actuators B: Chemical 156 (2), 662–667.
Joskowiak, A., Stasio, N., Chu, V., Prazeres, D.M.F., Conde, J.P., 2012. Biosensors & Bioelectronics 36 (1), 242–249.
Kamei, T., Paegel, B.M., Scherer, J.R., Skelley, A.M., Street, R.A., Mathies, R.A., 2003. Analytical Chemistry 75 (20), 5300–5305.
Kamei, T., Toriello, N.M., Lagally, E.T., Blazej, R.G., Scherer, J.R., Street, R.A., Mathies, R.A., 2005. Biomedical Microdevices 7 (2), 147–152.
Karakiulakis, G., Roth, M., 2012. Mediators of Inflammation , http://dx.doi.org/10.1155/2012/409580. (ID 409580).
Kenakin, T.P., 2009. Nature Reviews Drug Discovery 8 (8), 617–626.
Kiselyov, K., Shin, D.M., Muallem, S., 2003. Cellular Signalling 15 (3), 243–253.
Kostenis, E., Waelbroeck, M., Milligan, G., 2005. Trends in Pharmacological Sciences 26 (11), 595–602.
Lagerstrom, M.C., Schioth, H.B., 2008. Nature Reviews Drug Discovery 7 (4), 339–357.
Lefkowitz, R.J., 2007. Acta Physiologica 190 (1), 9–19.
Lipovsek, B., Joskowiak, A., Krc, J., Topic, M., Prazeres, D.M.F., Chu, V., Conde, J.P., 2010. Sensors and Actuators A: Physical 163 (1), 96–100.
Liu, K., Southall, N., Titus, S.A., Inglese, J., Eskay, R.L., Shinn, P., Austin, C.P., Heilig, M. A., Zheng, W., 2010. Assay and Drug Development Technologies 8 (3), 367–379.
Marshall, I.C., Owen, D.E., McNulty, S., 2006. Methods in Molecular Biology 312, 125–131.
Martins, S.A.M., Trabuco, J.R.C., Monteiro, G.A., Chu, V., Conde, J.P., Prazeres, D.M.F., 2012. Trends in Biotechnology 30 (11), 566–574.
Mundell, S.J., Benovic, J.L., 2000. Journal of Biological Chemistry 275 (17), 12900–12908.
Novo, P., Moulas, G., Chu, V., Conde, J.P., 2012. Lab-on-Chip prototype platform for ochratoxin A detection in wine and beer. In: Walczak, R., Dziuban, J. (Eds.), Proceedings of the 26th European Conference on Solid-State Transducers, Eurosensor, pp. 550–553.
Pereira, A.T., Novo, P., Prazeres, D.M.F., Chu, V., Conde, J.P., 2011. Biomicrofluidics 5, 1.
Piggott, M., Owens, J., O'Brien, J., Paling, S., Wyper, D., Fenwick, J., Johnson, M., Perry, R., Perry, E., 2002. Journal of Chemical Neuroanatomy 24 (3), 211–223.
Pimentel, A.C., Prazeres, D.M.F., Chu, V., Conde, J.P., 2008. Journal of Applied Physics 104, 5.
Schlyer, S., Horuk, R., 2006. Drug Discovery Today 11 (11–12), 481–493.
Scott, C.W., Peters, M.F., 2010. Drug Discovery Today 15 (17–18), 704–716.
Sewing, A., Cawkill, D., 2007. In: Bourne, H., Horuk, R., Kuhnke, J., Michel, H. (Eds.), GPCRs: From Deorphanization to Lead Structure Identification. Springer, Berlin Heidelberg, pp. 249–266.
Shoichet, B.K., Kobilka, B.K., 2012. Trends in Pharmacological Sciences 33 (5), 268–272.
Takahashi, A., Camacho, P., Lechleiter, J.D., Herman, B., 1999. Physiological Reviews. 79 (4), 1089–1125.
Thomas, P., Smart, T.G., 2005. Journal of Pharmacological and Toxicological Methods 51 (3), 187–200.
Vasilev F., Chun J.T., Gragnaniello G., Garante E., Santella L., PLoS One 7 (6), in press, http://doi.org/10.1371/journal.pone.0039231.
Zhang, J.H., Chung, T.D.Y., Oldenburg, K.R., 1999. Journal of Biomolecular Screening 4 (2), 67–73.
Zhang, R., Xie, X., 2012. Acta Pharmacologica Sinica 33 (3), 372–384.
Zwier, J.M., Roux, T., Cottet, M., Durroux, T., Douzon, S., Bdioui, S., Gregor, N., Bourrier, E., Oueslati, N., Nicolas, L., Tinel, N., Boisseau, C., Yverneau, P., Charrier-Savournin, F., Fink, M., Trinquet, E., 2010. Journal of Biomolecular Screening 15 (10), 1248–1259.